UCLA
UCLA Previously Published Works

Title
Atomic layer etching of metals with anisotropy, specificity, and selectivity

Permalink
https://escholarship.org/uc/item/9074j7nt

Journal
Journal of Vacuum Science & Technology A Vacuum Surfaces and Films, 38(4)

ISSN
0734-2101

Authors
Sang, Xia
Xia, Yantao
Sautet, Philippe
et al.

Publication Date
2020-07-01

DOI
10.1116/6.0000225

Peer reviewed

eScholarship.org Powered by the California Digital Library
University of California

Atomic Layer Etching of Metals with Anisotropy, Specificity and Selectivity

Running title: Atomic layer etching of metals with anisotropy, specificity and selectivity
Running Authors: Sang et al.

Xia Sang [1], Yantao Xia [2], Philippe Sautet [2,3] and Jane P. Chang [1,2,a)]

[1] Department of Material Science and Engineering, University of California, Los Angeles, California 90095
[2] Department of Chemical and Biomolecular Engineering, University of California, Los Angeles, California 90095
[3] Department of Chemistry and Biochemistry, University of California, Los Angeles, California 90095

a) Electronic mail: jpchang@ucla.edu

In this work, a special focus is given to ALE of metals, since this is a relatively new field but is expected to grow rapidly given the major advancements potentially enabled via metal incorporation throughout the manufacturing process of integrated circuits. The impact of John Coburn's work on the development of atomic layer etching processes is analyzed with a focus on ion energy and the neutral-to-ion ratio. To realize atomic precision in removing etch-resistant materials with complex compositions or structures, the surface reactivity would replace etch rate as the parameter of interest to control the chemical contrast needed for selectivity. The desirable etching anisotropy dictates the usage of directional ions. John Coburn's work on ion-enhanced etching of Si serves as an example that a fine control of the ion energy and neutral-to-ion ratio could be the gateway of reactivity control, which is demonstrated with recent progress on thermal-plasma ALE of Ni. The effect of surface reactivity is studied from first principle atomistic calculations and confirms the experimental findings.

I. INTRODUCTION

The world has witnessed the most rapid outburst of sensor technology in the recent decade, with a global mobile market growing by more than ten times into a multi-billion-dollar industry[1]. These sensor integrations at various levels enabled the Internet of Things (IoT) and Internet of Everything (IoE), including smart home, autonomous cars, wearable health and wellness devices, and point-of-use manufacturing. The fuel of such exponential increase, and the backbone of the infrastructure, is the ever-progressing evolution of integrated circuits that includes transistors and memory devices at nanometer scales. Amongst the hundreds of steps involved in the manufacturing process, etching plays a crucial role since it determines the quality of pattern transfer and feature registration. The importance of this step was emphasized by John Coburn throughout his career: "…without the highly anisotropic etching provided by this critical process, high density integrated circuit manufacturing would not be possible" [2].

To sustain the functional device performance requirement with continuous transistor miniaturization, novel architectures were developed and implemented. The need for complex topographies and materials integration in next-generation logic and memory devices imposes stringent requirements on processing uniformity and consistency. Amongst many emerging challenges in developing such processes, two related to metal patterning stand out as the most critical: (1) an anisotropic patterning process to shape the thin metal absorbers on the extreme ultra-violet (EUV) mask so it can be used to replace multiple immersion photomasks and produce better features with greater pattern transfer fidelity and (2) an anisotropic patterning process to etch magnetic multi-layers so that their integration in spintronics or other non-volatile devices can be more effective.

In fact, the era of metals, referring to the introduction of complex metal stacks in enabling technologies, represents a real challenge in materials integration since many of these metals are chemically inert. Metals offer superior physical properties such as high electrical and thermal conductivities – traits desirable for microelectronics integration. Additionally, the manipulation of magnetism enables many novel applications due to the growing interests in the area of spintronics and magnetic memory devices, where the non-volatile nature of magnetization switching can be used to significantly reduce the power requirement. However, in contrast to the rapid increase in application needs, metal patterning at the nanometer scale remains largely unsolved, as many of these metals are etch-resistant.

Creative solutions have been developed to circumvent some of these challenges. One example is the ion beam etching (IBE) of the magnetic tunneling junction (MTJ) stacks, which is capable of realizing vertical sidewall on complex multi-element thin film stacks using Ar sputtering with the specialized setup of stage rotation and tilting (e.g., etching with 45° wafer-tilted IBE and over etching with 25° wafer tilt at a rotating speed of 10 to 100 rpm)[3, 4]. This approach, while effective, has limit for generalization since the rotation setup only applies to cylindrical geometry and the higher aspect ratio features make it difficult for the ions to reach the bottom sidewall. To realize metal etching with sub-10 nm fidelity over complex surface geometries, a generalizable gas phase patterning technique with extreme precision and high selectivity needs to be developed.

II. Impact of John Coburn's Work on ALE

The work of John Coburn on ion-enhanced chemical etching have inspired and influenced the field for several decades and continues to provide insights on novel topics such as metal etching motivated above. The most well-known is his seminal work with Harold Winter [5] that shows the combined chemical and physical effect on the etching of polysilicon, as evident by the citation summary in Figure 1. The inset in Figure 1 shows the original data establishing the notion of ion-and-neutral synergy the etch rate of silicon was measurable but small by either XeF_2 gas at a flux of 6×10^{15} molecules/cm^{2}s or a 450 eV Ar ion beam at a flux of 1.6×10^{14} ions/cm^{2}s, but was significantly enhanced with both Ar ions and XeF_2 gas were used. The enhancement originated from a combination of various effects, including preferential dissociative chemisorption of XeF_2 on defect sites created by ion bombardment, ion-induced fragmentation of XeF_2 from momentum transfer, and collision-promoted cleaning of the gas-adsorbed surface. This original work led to many other studies where a spontaneous reaction with reactive neutrals (chemicals) led to the formation of volatile products, while an inert ion with an energy higher than sputtering threshold energy can create reactive site and facilitate the removal of the reaction products through momentum transfer.

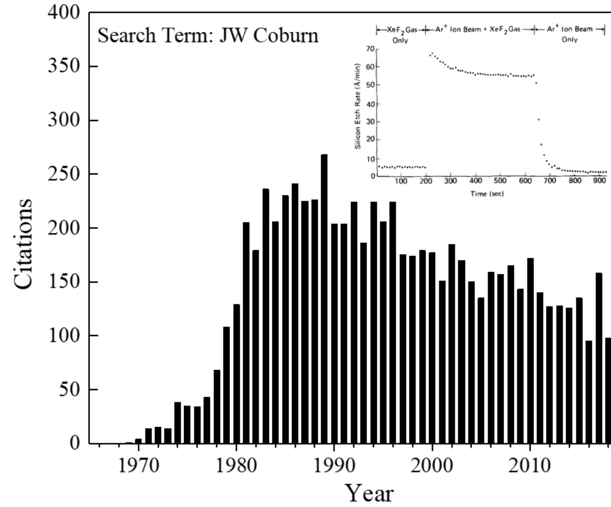

Figure 1. Citation record of John Coburn's publication with the inset showing the original data that clarified the synergistic effect between ions (Ar^+) and reactive neutrals (XeF_2) on etching silicon. Inset reprinted from Coburn, J.W. and H.F. Winters, J. Appl. Phys. 50, 3189 (1979) with the permission of AIP Publishing.

In recent years, the ever-shrinking dimensions of the electronic devices dictated the development of an atomic layer etching (ALE) process to further extend the limit of patterning capability. While largely leveraging the same concept from RIE, ALE differs in that the reactants are introduced in a time-separated and cyclic manner, thereby limiting the surface reactions on the very top exposed layer(s) of the target material. Various ALE chemistries have been developed for a considerably large selection of materials, including semiconductors [6, 7], dielectrics[8, 9], metals [10, 11] and polymers [12]. Some of the state-of-the-art ALE chemistries are capable of removing less than 1 Å of material per cycle [13, 14]. In fact, an "ALE synergy" parameter was introduced as an effective means to account for the behavior unique to the reactant–material combination for various systems and was described as "inspired by the ion-neutral synergy concept introduced in

the 1979 paper by Coburn and Winters" [15]. A list of reported ALE chemistries for metals are summarized in Table 1, including both thermal and plasma processes.

Table 1. Reported metal ALE chemistries

Metal	Plasma	Chemistry	Comment	Etch Rate (nm/cycle)	Reference
Cr	Cl_2 & Ar	-	Plasma ALE	0.2	11
Pd	O_2	Formic acid	Thermal-plasma ALE	1.2	16
Ta	O_2	Ethanol			17
Ru	O_2	Ethanol			17
Pt	O_2	Formic acid	Thermal-plasma ALE	0.5	16
	O_2	Ethanol			17
Co	-	Cl_2 & hfac/acac	Thermal ALE	1.6	10
	O_2	Formic acid	Thermal-plasma ALE	2.8	16
Cu	-	O_2/O_3 & hfac	Thermal ALE	0.1	18
	O_2	Formic acid	Thermal-plasma ALE	3.7	16
Fe	-	Cl_2 & acac	Thermal ALE	5.0	19
	O_2	Formic acid	Thermal-plasma ALE	4.2	16
W	-	O_2/O_3 & BCl_3 & HF	Thermal ALE	0.3	20
	Cl_2 & Ar	-	Plasma ALE	0.2	15

Given that many metals are chemically inert, an easily accessible process would likely be a physical one (e.g., sputtering), which translate to non-specific removal of surface species, including the target material as well as the surrounding materials. In fact, the focus of the field is shifting from pursuing higher etch rate to greater selectivity, which means that the thermodynamics, in addition to the kinetics, of the etching chemistries, must be emphasized.

III. Effect of Neutral-to-Ion Ratio and Ion Energy

One way to tackle the etching selectivity is to tailor the etching rates by adjusting the neutral-to-ion ratio in the etching process. Though it is not always possible to tune the neutral to ion ratio inside a plasma reactor due to the relatively low degree of ionization

(~1%), it is feasible to separately control the neutral and ion fluxes in a molecular beam system (similar to the beam experiments in Coburn's work). Figure 2 (a) is an adapted illustration of the etching yield (normalized rate) dependence on neutral-to-ion ratio and ion energy, based on experiemtally determined results (Figure 2(b)). The etching yield increases rapidly (~10 x) at low flux ratio and reaches a plateau at higher flux ratio. The small etching yield is limited by the available reactive atom flux on the surface, while etching yield saturation at a high flux regime is limited by the ion flux [21]. The dependence of overall etching yield on the neutral to ion ratio is analytically expressed as [22]:

$$Y_{tot} = Y_{spu} + (\beta - Y_{spu}) \frac{sR}{sR + n\beta},$$

where Y_{tot} is the overall etching yield, Y_{spu} is the etching yield from physical sputtering, n is the number of ions generated per reaction, β is the ion-enhanced reaction probability, s is the sticking coefficient, and R is the neutral-to-ion ratio. Since both s and β increase linearly with $E_{ion}^{1/2}$ [22], the overall etching yield also increases with increasing ion energy. Relating back to Coburn and Winter's original work cited in Figure 1, where 450 eV Ar ions and an estimated neutral-to-ion flux ratio of ~ 100 were used, the process was clearly in the RIE regime, where a combination of high neutral-to-ion ratio and a high ion energy is often used. To realize an ALE process, where a self-limiting reaction step must be present to enable the precision in removing materials, the physical "sputtering" effect should to be minimized. This can be achieved by lowering the ion energy to be below the sputtering or etching threshold energy. The chemical effect from the ions also needs to be modulated so that the reaction leads to modification, not removal, of materials. In other words, the neutral-to-ion flux ratio should be kept low, to a point where the reaction

might not lead to the formation of volatile products. In fact, a neutral-to-ion ratio of *zero* maybe ultimately what is needed in ALE, where the role of the chemically reactive ion (with energy below threshold) is to create a chemical contrast in the material that leads to a subsequent self-limiting reaction.

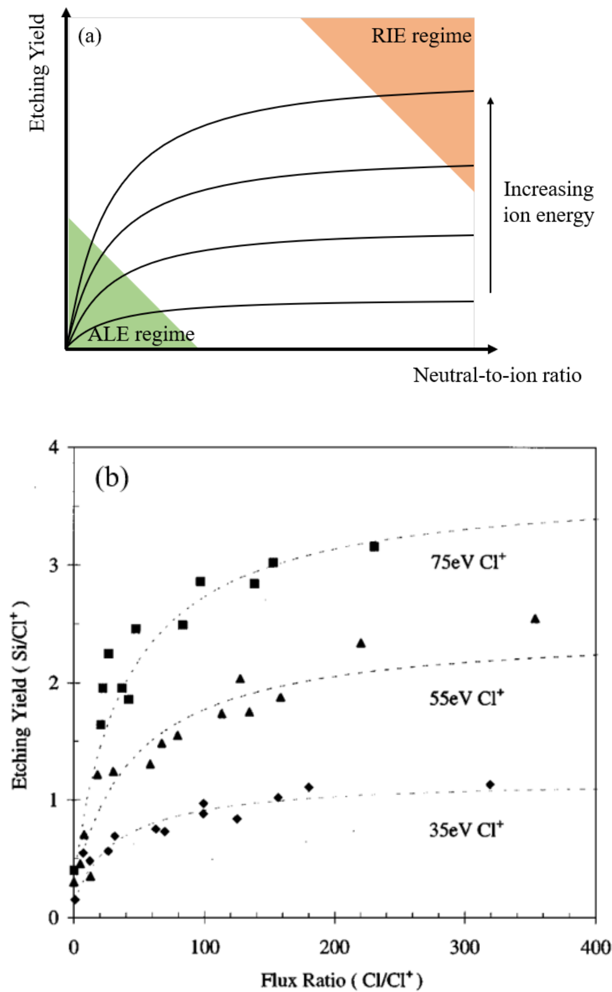

Figure 2. (a) A qualitative expression of the effect of the neutral-to-ion ratio and ion energy on the etching yields of materials, using reactive ions and neutrals. The generalized regimes for RIE and ALE are colored. (b) An experimental confirmation of (a) using a models developed for Cl^+ and Cl etching of polysilicon [23]. Reprinted with permission from Chang, J. P. and Sawin, H. H., JVST A 15, 610 (1997); https://doi.org/10.1116/1.580692. Copyright 1997 by the American Vacuum Society.

To ensure high (ideally infinite) selectivity on the target material, virtually no thickness reduction is allowed during individual steps. More specifically, chemical reactions should not be spontaneous during the neutrals-only stage or at least reaction products should not be volatile, and inert ions should have kinetic energies lower than the sputtering threshold of the target material. Thickness reduction is only *enabled* via the chemical contrast from the ion, rather than its kinetic energy, through means such as altering thermodynamic favorability or enabling reaction product volatility. An example of this approach would be a newly proposed plasma-thermal ALE process [24]. The standalone physics component of the process utilizes reactive ions with energy lower than the sputtering threshold of target material, resulting in zero thickness decrease. The standalone chemistry component of the process does not etch the target material either due to the fact that non-modified region is thermodynamically unfavorable to react with incoming molecules. The combination of the two components enabled etching as reaction is favorable on the chemically modified region, the thickness of which is not decreased by ion sputtering.

Most of the reported RIE literature have involved the use of inert ions as the carrier of kinetic energy for surface bombardment, as the inertness eliminates the complication of potential addition of surface reactions. In etching *single elemental species*, such as Si or a metal, physical sputtering is the only mechanism possible for reactions with inert ions since they do not form chemical bonds with the surface elements. The sputtering yield is dictated by the momentum transfer to the surface [22]:

$$Y = A\left(\sqrt{E_{ion}} - \sqrt{E_{threshold}}\right),$$

where Y is the sputtering yield, E_{ion} is the ion energy, $E_{threshold}$ is the sputtering threshold energy, and A is a projectile–target combination dependent constant. This is

illustrated in Figure 3 (a) as a physical sputtering process. When reactive gases are used along with the inert ions to enhance the etching, a different A and threshold energy can be determined, but the functional form remains the same (in Figure 3(a) as ion-enhanced etching).

In plasma etching more complex materials such as *metal oxides*, where simultaneous etching and deposition occur, a comprehensive model has been developed, based on mass and site balance near the surface region, to account for the ion energy dependence involving more than one critical threshold energies:

$$R_t = \frac{J_e^2 Z_{es} Z_{ep} - J_d^2 Z_{ds} Z_{dp}}{J_e Z_{ep} + \frac{J_d^2 Z_{ds} Z_{dp}}{D_p} + \frac{J_d J_e Z_{ds} Z_{ep}}{J_i C_p (E_{ion}^{0.5} - E_{th,p}^{0.5})} + J_d Z_{ds} + \frac{J_d J_e Z_{ds} Z_{ep}}{D_s} + \frac{J_e^2 Z_{es} Z_{ep}}{J_i [A_s (E_{ion}^{0.5} - E_{th,s}^{0.5}) + B_s (E_{ion}^{0.5} - E_{tr,s}^{0.5})]}}$$

where *J* denotes species fluxes, *Z* represents the product of volume removed/added per reactive species and the reactive sticking probability, A, B, C are volumes removed, *D* is the deposition rate. E_{ion} is the ion energy, $E_{th,s}$ is the substrate etching threshold energy, $E_{tr,s}$ is the substrate transition energy (in the case of etching metal oxides, close to the dissociation energy of metal-oxygen bonds), and $E_{th,p}$ is the polymer etching threshold energy. The subscripts *e*, *d*, *s*, and *p* represent etching, deposition, substrate, and polymer, respectively [25]. This is illustrated in Figure 3(b), in comparison to the energy dependence of a purely physical sputtering process.

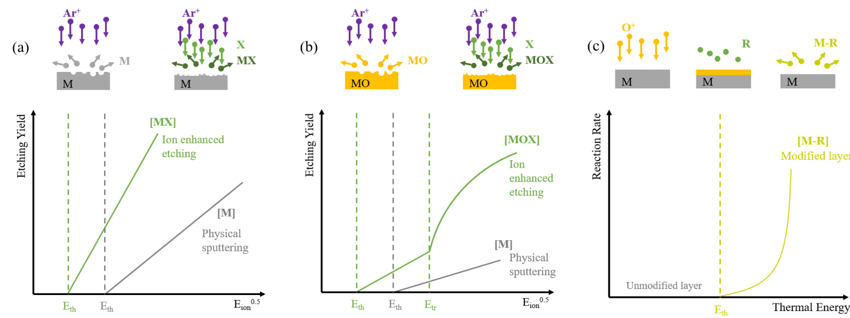

Figure 3. Etching yield as functions of incoming ion energy for (a) metal and (b) metal oxide. Comparing to (c) a conversion-etch process of metal where low energy oxygen ions converts the surface to oxide, for subsequent chemical reactions.

To realize atomic layer etching of metals with tight dimensional control, an extra layer of complexity needs to be considered, taking advantage that reactive ions are capable of chemically modifying the surface at an energy level below the sputtering threshold. Figure 3 (c) illustrates the concept of separating the physical and chemical effects for high precision and selective patterning. In the case of etching Si, instead of utilizing the binding energy difference between halogenated silicon layer and pristine silicon layer as demonstrated in Coburn's work, reaction thermodynamics between oxidized silicon and a highly selective etchant such as HF could be used. Namely, low energy directional oxygen ions would be used to convert the surface layer from silicon to silicon dioxide, and subsequent gas phase HF vapor could remove completely and only the oxidized layer, leaving the silicon layer underneath in a new and pristine surface state, terminated with hydrogen. This can be generalized to other metals, in that the chemical reactivity of ions is used to tailor the surface modification/conversion to form a metal oxide layer and any adventitious sputtering is suppressed. This distinction is especially important for realizing highly selective etching on etch-resistant materials such as transition metals or

noble metals since sputtering leads to damage and poor selectivity with respect to surrounding materials.

In the next section, chemical modification of Ni is used as an example to show the modification effect of low energy reactive ions. A surface layer of Ni (~5 nm) is purposefully transformed from metallic Ni to NiO via low energy oxygen ion exposure, in order to access new reaction pathways exclusively for NiO removal but not Ni. In fact, the chemical contrast between surface NiO and bulk Ni leads to almost infinite etching selectivity, in a way similar to the attainable selectivity of etching SiO_2 and Si using HF.

IV. ALE of Nickel, an Example

The difference in electron configuration between metals and their oxides have been widely studied for various purposes. For the purpose of realizing selective chemical etching, it has been shown that localizing electrons on metal surfaces via oxidation is a viable way of facilitating the removal of these modified surface layers [26]. It has been demonstrated that organic chemistries can selectively remove the surface metal oxide layer without retain with the underlying pristine metal material [27]. Since the selectivity is defined solely from the oxidation process, the controllable formation of the surface oxide layer is thus critical in realizing the subsequent material removal, including both selectivity and directionality. It is noted that UV/VUV radiation effect is considered not predominant, as the grain size of the Ni thin film used in this experiment is on the order of one to tens of nanometers. The contribution of surface roughness from UV/VUV radiation is equally, if not less noticeable from initial morphology.

To assess the controlled surface oxidation, a low energy plasma oxidation process (30 mTorr, 500 W source power, no applied substrate bias or heating, 2 minutes) was used to convert the surface of 30~40 nm Ni thin films into oxides. Surface atomic composition and chemical bonding configuration before and after oxidation was obtained using X-Ray Photoelectron Spectroscopy (XPS, Kratos XPS Axis Ultra DLD, monochromatic Al Kα source with a pass energy of 20 eV) and film thickness change was measured by Scanning Electron Microscope (SEM, FEI Nova 600 with 10 keV electron beam) and Transmission Electron Microscope (TEM, FEI Titan S with 200 keV electron beam).

As shown in Figure 4, the Ni sample was first sputter-cleaned by 4 keV Ar ions to remove the native oxide layer and establish a baseline for compositional analysis. It was then exposed to an oxygen plasma *ex-situ* for 2 minutes. Due to the ambient exposure, some adventitious carbon was observed, which caused signal attenuation of other elements. Without the applied substrate bias, the ion energy was about the plasma self-bias potential, ~10 eV, which was lower than the sputtering threshold of Ni which was reported to be ~16 eV [28]. It is thus expected that main effect of these low energy ions was oxidation and no significant sputtering due to the small populations of ions at the high energy tail of the ion energy distribution function. The formation of NiO is confirmed from the *ex-situ* XPS analysis where the signal intensity of metallic Ni (852.6 eV) is considerably reduced, and that of NiO (854.1 eV) is greatly increased. Increase in signal intensity is also noticed for $Ni(OH)_2$ (855.8 eV) and satellite features (858.1 eV and 859.9 eV). With the known photoelectron mean-free paths of Ni and NiO and the atomic sensitivity factors for Ni and O, the oxide layer thickness can be calculated using the following equation: $I_{ox}^{t}/I_{Ni}^{t} = I_{ox}^{\infty}\left[1-\exp\left(-\frac{t_{ox}}{\lambda_{ox}^{o}\sin\theta}\right)\right]/I_{Ni}^{\infty}\exp\left(-\frac{t_{ox}}{\lambda_{ox}^{Ni}\sin\theta}\right)$, where I_{ox}^{t} and

I_{met}^{t} are the integrated intensity of O1s and Ni $2p_{3/2}$ peaks, tox is the oxide thickness, λ_{ox}^{o} are λ_{ox}^{Ni} are the photoelectron mean-free paths for O 1s and Ni 2p and θ is the angle between the sample surface and the electron analyzer, 90° in this work. The ratio $I_{ox}^{\infty}/I_{Ni}^{\infty}$, has been experimentally measured to be 0.17, and confirmed with theoretical calculation [29]. The mean-free path O 1s and Ni 2p photoelectrons in the oxide were determined to be 2.1 nm and 1.7 nm, respectively, using the relation of $\lambda = 2170/E^{2} + 0.72(aE)^{0.66}$, where E is the electron kinetic energy in eV and a is the molecule size in nm as derived from the relation $\rho Nna^{3} = 10^{24} A_{0}$. Therefore, the oxide thickness was determined to be ~ 6 nm.

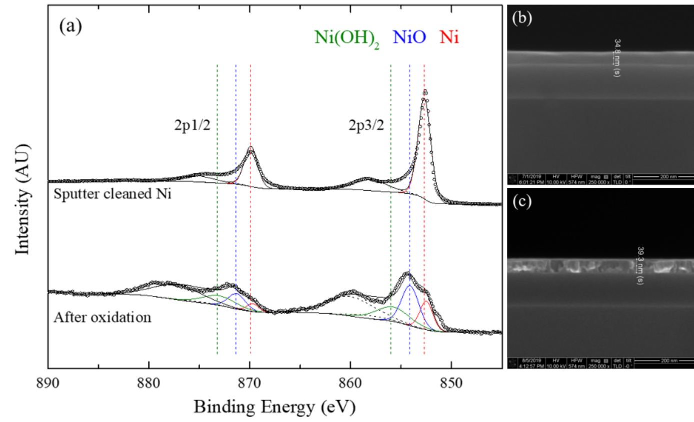

Figure 4. (a) Ex-situ XPS detail scan of Ni2p and SEM cross-sectional image for Ni blanket sample (b) before and (c) after 2 minutes of oxygen plasma exposure, 500 W power, 0 W applied bias.

The calculated NiO thickness is corroborated by the SEM analysis, where a thickness increase of ~5 nm is measured on the oxidized Ni thin film comparing to the non-oxidized surface. It is noted that the formation of a native oxide layer of ~2 nm takes ~24 hours in the ambient condition, which is considerably longer than the time required to transfer the post-oxidation samples for ex-situ XPS measurements. Figure 5(a) shows Ni

2p, C 1s and O 1s spectra with various oxidation time under the same plasma conditions. The amount of Ni in its metallic, oxide, hydroxide states are shown in Figure 5(b), where it is clear that more oxides are formed with a longer oxidation time but the relative concentration between hydroxides and oxides began to change at longer oxidation time (1 to 4 min). Figure 6(a) shows Ni 2p, C 1s and O 1s spectra with various substrate bias power applied for 30 seconds for the same plasma oxidation conditions. The amount of Ni in its metallic, oxide, hydroxide states are shown in Figure 6(b), where a nearly monotonic increase in the amount of oxidized nickel was observed with increasing substrate bias (0 to 20 W). Since the formic acid chemistry in the gas phase is only reactive with oxidized nickel, the extent of oxidation translates to the attainable etching rates, while realizing a very high selectivity [30]. The targeted reaction in directionally oxidized region would lead to directional removal, where the reaction viability is determined by the thermodynamics of the reaction, not the energy of the ions. Finally, since gas phase etch product identification and characterization by in-situ mass spectrometry analysis were attempted but not successful due to both the low etch rates and small concentrations of the reaction products, computational insight is therefore needed to elucidate the reaction pathways and products.

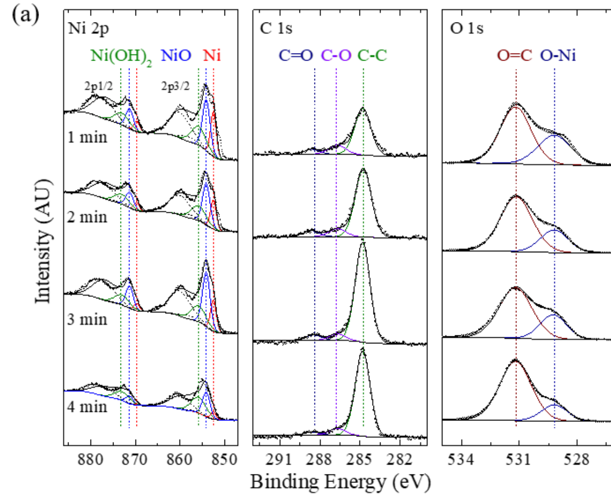

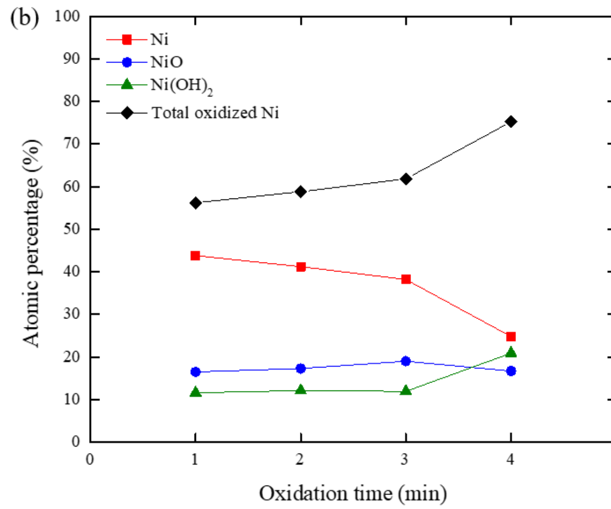

Figure 5. (a) XPS of Ni 2p, C 1s and O1s, and (b) the relative atomic percentage of different nickel chemical states as a function of the oxidation time. All experiments started with a 15 sec Ar sputtering, followed in-situ oxidation at 500 W power 0 W applied bias.

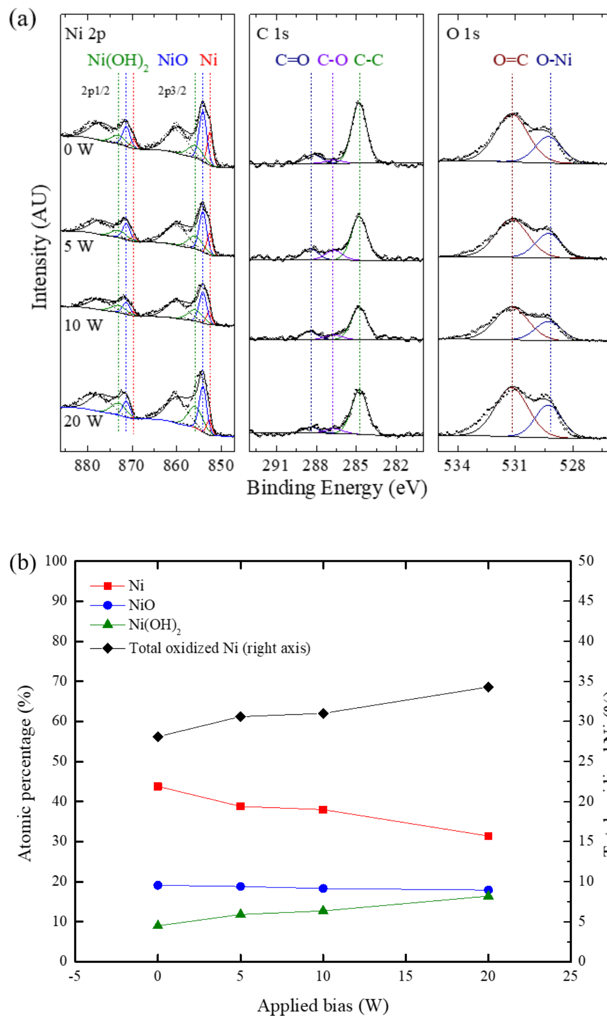

Figure 6. (a) XPS of Ni 2p, C 1s and O1s, and (b) the relative atomic percentage of different nickel chemical states as a function of the substrate bias. All experiments started with a 15 sec Ar sputtering, followed in-situ oxidation at 500 W power for 30 seconds.

To provide molecular scale understanding and determine the thermodynamic balance and reaction products during formic acid etching of oxidized nickel, density functional theory (DFT) calculations were performed. The PBE exchange correlation functional was used using the VASP code [31-35]. One-electron functions are developed on a basis set of plane-waves, with an energy cutoff at 400 eV. The energies and forces are converged to 1×10^{-6}

eV, and 2×10^{-2} eV/Å, respectively. The Gibbs free energies of reaction are evaluated at a specific processing temperature, 80°C and at a pressure of 350 torr [36].

Three nickel surfaces, (100), (111), and (211), were selected since they are representative of facet and edge sites present on polycrystalline surfaces. To create an oxidized nickel surface, atomic oxygen was chemisorbed on nickel. At the coverages of interests, the most stable phase is surface adsorption (overlayer). The metastable structures likely to be present after oxygen adsorption are probed by placing oxygen in the sublayer interstitial sites (sublayer structures). In a real oxidation process, some overlayer sites are likely to be populated first due to the kinetic barriers of accessing the sublayer sites, therefore, a mixed structure presenting overlayer and sublayer sites is also included. Note that these structures model initial oxidation of the Ni surface and are much thinner than the experimental NiO layer on Ni. They should nevertheless provide general insights on the thermodynamics and pathway for the etching process. Figure 7 shows the structures for the three surfaces. The sites on the stepped (211) surface deserve some explanation. While the overlayer and mixed structures initially had different site occupation, after relaxation they became very similar. Two types of oxygen atoms are present, namely 4-coordinated (4c) and 3-coordinated (3c). The overlayer structure has one 4c O atom and two 3c O atoms. The mixed structure shows two 4c O atoms (one in a square planar 4-fold hollow site, one in a tetrahedral interstice site) and one 3c atom (in a three-fold hollow terrace site). The sublayer structure has only 3c O atoms.

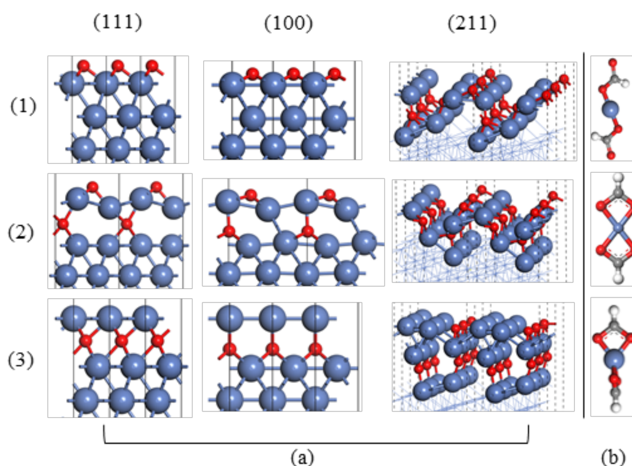

Figure 7. (a) Illustration of the relaxed structures of (100), (111), (211) surfaces with (1) overlayer, (2) mixed, and (3) sublayer oxygen adsorption. The (111) and (100) surfaces are shown in side view, the (211) surface is shown in perspective. (b) from top to bottom: monodentate, bidentate planar, bidentate tetrahedral geometry for the Ni di-formate complex. The bidentate planar geometry is calculated to be the most stable of all, being 0.41 eV lower in energy than the tetrahedral stereoisomer, which is in turn 0.99 eV lower in energy than the monodentate structure.

To study coverage effects, three scenarios are considered here, represented in the chemical reactions below:

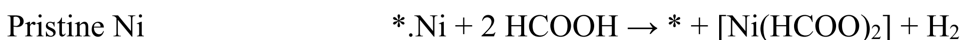
Pristine Ni $*.Ni + 2\ HCOOH \rightarrow * + [Ni(HCOO)_2] + H_2$

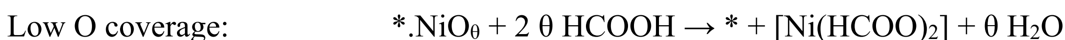
Low O coverage: $*.NiO_\theta + 2\ \theta\ HCOOH \rightarrow * + [Ni(HCOO)_2] + \theta\ H_2O$

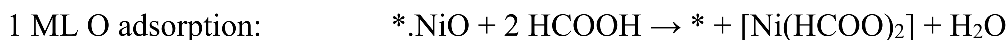
1 ML O adsorption: $*.NiO + 2\ HCOOH \rightarrow * + [Ni(HCOO)_2] + H_2O$

The monolayer (ML) coverage is redefined with respect to the number of nickel atoms exposed to modifiers (O). For p(2×1) cells used in (111) mixed structure, for instance, two nickel atoms are exposed, hence 1ML corresponds to 2 oxygen atoms, one in the overlayer and the other in the sublayer. The θ values of low coverage cases are specified in Table S1.

Since no experimental characterization of the gas phase nickel di-formate complex $[Ni(HCOO)_2]$ is available, various structures were considered with DFT, and the most stable one is used in the energy calculation. The formate structure candidates are shown in Figure 7 (on the right from top to bottom: monodentate, bidentate-planar, bidentate-tetrahedral). The monodentate structure corresponds to the configuration in solid state nickel formate dihydrate [37] but it is not stable in the gas phase. The bidentate planar structure is the most stable one. Note that this is a 16-electron square planar structure, common for d^8 metal complexes.

The reaction energy for the simpler 1ML case is given by the following equation.

$$\Delta G_{et} = \left[G_{l+1,\mathrm{NiO}} - G_{l,\mathrm{Ni}} + \left(\mathring{n}_{\mathrm{Ni}} G_{[\mathrm{Ni(HCOO)_2}]} + \mathring{n}_{\mathrm{Ni}} G_{\mathrm{H_2O}} - 2\mathring{n}_{\mathrm{Ni}} \cdot G_{\mathrm{HCOOH}}\right)\right] \cdot \frac{1}{\mathring{n}_M}$$

The derivation of the reaction energy for the low coverage limit using the layer-removal model is given in Eqn. S3. Figure 8 shows the reaction energy of various activated surfaces considered (per Ni atom removed). Most notably, for the 1ML case, oxygen activated nickel surfaces can be favorably etched via formate chemistry, consistent with the experimental work. Etching of the pristine nickel surface to produce Ni diformate and gas phase hydrogen is calculated to be endergonic by 1.7 eV and is hence highly unlikely. This is consistent with our experiments where the unmodified clean nickel is not etched. Purple bars on Figure 8 show that the etching reaction for Ni surfaces modified by a low coverage of oxygen adatoms is also thermodynamically unfavorable by more than 1.5 eV. Hence only surfaces modified by a high coverage of O atoms, with occupation of subsurface sites and the formation of a surface NiO layer, result in a favorable etching reaction with formic acid, in agreement with experiments. Note that the favorable etching

reaction for these oxidized surfaces is not resulting from a greater stability of the products (Ni di-formate and water), since the energies are already normalized with respect to the number of metal atoms, but from a reduced binding of the Ni atoms in the "reactant" surface.

The site dependence trend is quite complex. For (111), increasing access to sublayer sites increasingly destabilizes the surface, while (100) and (211) surfaces are not significantly destabilized by occupying a fraction of the sublayer sites in a mixed adsorption structure. (100) and (211) results indicate that occupying the sublayer sites using low energy oxygen ions can make the etching reaction favorable. A closer look at Figure 8 reveals that etch becomes more favorable when Ni atoms in the top layer have a longer bonding distance with the layers underneath due to occupation by oxygen atoms in the sublayer. In particular, all the sublayer structures show a large vertical relaxation of the top layer, moving away from the bulk, while the mixed and overlayer structures still have one or more Ni atoms at short distance from the underlying metal. It seems to suggest that the geometry distortion caused by the oxygen modifier provides a favorable driving force. However, a more detailed search of the configuration space is required to validate this. Note that overall (211) has a higher reaction energy compared with (100) and (111). This is due to the fact that while (211) surface itself has a higher surface energy, occupying the under-coordinated sites on the edge initially stabilized the surface, to a higher extent than that on (100) and (111), where the terrace atoms have a higher coordination number. These results suggest that site specificity can play a role in atomic layer etching of surface species.

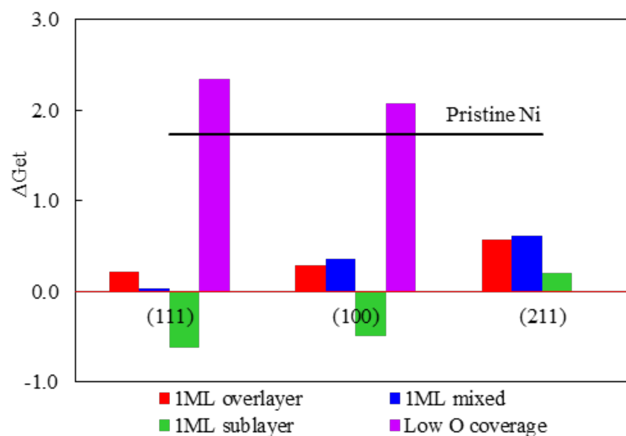

Figure 8. Etching reaction energies (ΔGet in eV) of oxidized nickel (111), (100), and (211) surfaces using a layer-by-layer removal model (negative values indicating a favorable etching, see Supplemental Information), normalized to one Ni atom removed. Low oxygen coverage does not result in a favorable etch, as indicated by positive reactions energies of over 2 eV. Sublayer sites significantly reduce the energy cost, in some cases resulting in a favorable etch, as observed experimentally. The energy level for a pristine nickel surface (1.74 eV, black line) is calculated with the Ni bulk formation energy since the same surface is exposed if the entire atomic layer of nickel is etched and removed.

The feasibility of low energy oxygen ions from a plasma specified above to convert a metal to a metal oxide surface without physical sputtering, followed by formic acid reaction to form volatile reaction products, is therefore established. The effect of modification from low energy oxygen ions could be further leveraged as directionality, thereby enabling anisotropic chemical activation in selected open areas of a pattern. Example shown in Table 2 illustrates the effectiveness of such an ALE process. Starting with a 40 nm Ni film that was patterned with a hard mask of SiO_2 lines (SiO_2 thickness = 95 nm, line width = 125 nm, and line pitch = 1 μm, initial sidewall angles of 60-80°), low energy oxygen plasma was used to tailor the formation of nickel oxide, followed by the nickel oxide removal with formic acid vapor exposure. The zoom-out TEM images

confirm the process uniformity (over at least hundreds of nanometer), while the EDS mapping of Ni shows an 87° final sidewall angle. Ni was completely removed in all exposed region, while slight variations in the sidewall profiles were noted from the elemental mapping by electron dispersion spectroscopy (EDS). These variations may be attributed to the grain size and grain boundary effects, which is beyond the scope of this current work but an important aspect to be researched further.

Table 2. TEM images of patterned Ni treated after 6 cycles of ALE (plasma oxidation-formic acid exposure), showing long range uniformity and etch anisotropy.

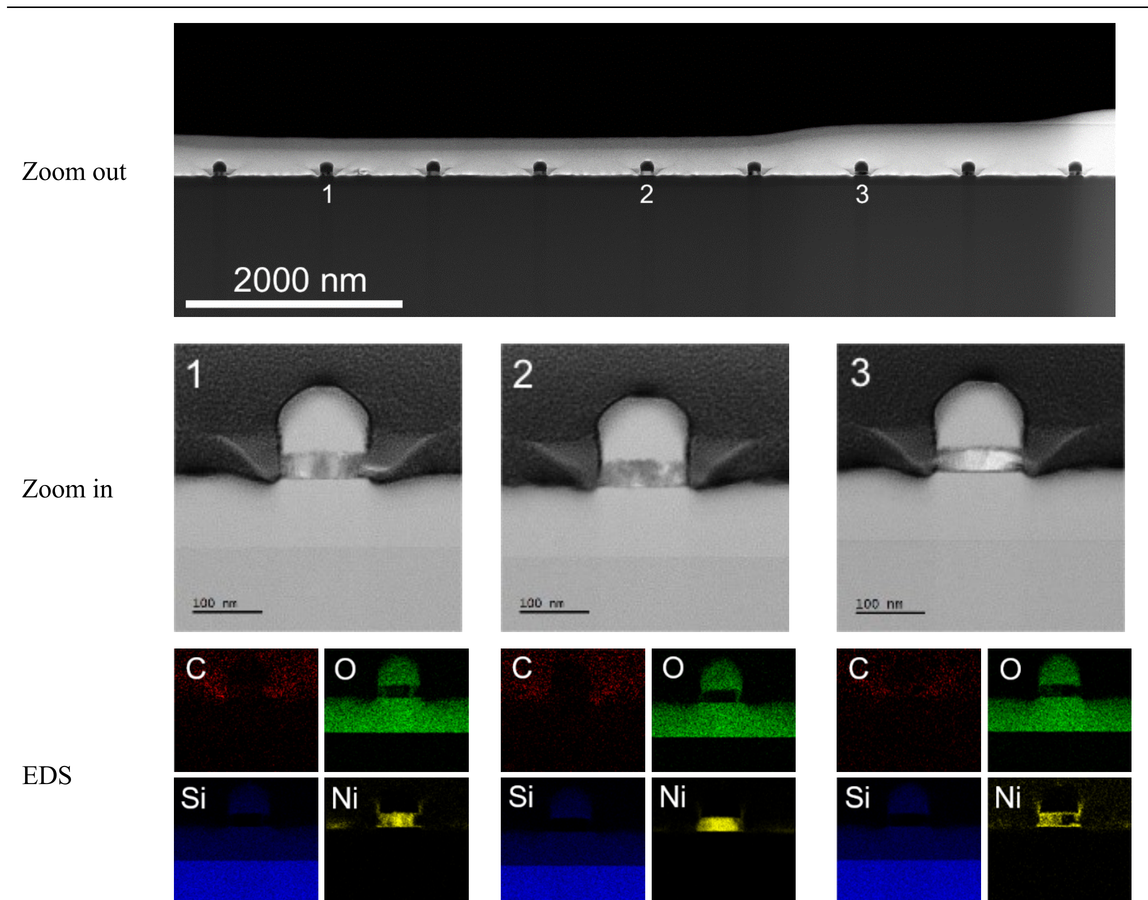

To refine the control of surface oxide layer formation, a mono-energetic and reactive ion source would be ideal since the narrower ion energy distribution would result in a more clearly defined oxide layer, which can translate to a greater precision in atomic layer

etching. The intrinsic directionality of oxygen ions leads to a directional formation of NiO with the presence of hard masks, which ultimately results in an anisotropic removal of the oxides.

V. SUMMARY

This work highlights the effect of low energy reactive ions and low neutral to ion ratios on atomic layer etching, the potential of which can be fully explored to tailor the surface reactions and selectivity. The work done by Coburn and Winters on chemical enhanced ion beam etching of polysilicon was used to introduce the main reaction mechanisms, with the focus on the etching dependences on in energy and neutral to ion ratios. In other words, reactive ion etching and atomic layer etching can be considered interrelated but only accessible at specific ion energy range and neutral-to-ion ratios. Building upon this concept, a general process is suggested to be expandable for future generation patterning processes that involve less-studied materials with tighter dimension constraints. Ion-thermal ALE of metals is motivated and discussed, in combination with first-principle calculations and confirmation, to demonstrate how surface reactivity and selectivity, instead of etch rate, is the focus of realizing nanometer-level patterning on etch-resistant materials.

ACKNOWLEDGMENTS

The authors acknowledge the financial support from the Semiconductor Research Corporation (2018-NM-2802), National Science Foundation (1805112), Lam Research, and Center of Design-Enabled Nanofabrication (C-DEN). The authors thank Dr. Changju

Choi and Dr. Tristan Tronic at Intel as well as Dr. Nathan Marchack at IBM for sample preparation and fruitful discussions. Yantao Xia and Philippe Sautet acknowledge UCLA IDRE for computational resources on the Hoffman2 cluster. The authors thank Dr. Mingjie Xu at UC Irvine for acquiring TEM images.

Reference

1. Deloitte, Global Mobile Consumer Trends, 2nd edition, (2017).
2. J. W. Coburn, presented at the APS Annual Gaseous Electronics Meeting Abstracts, (2003).
3. W. Boullart, D. Radisic, V. Paraschiv, S. Cornelissen, M. Manfrini, K. Yatsuda, E. Nishimura, T. Ohishi and S. Tahara, presented at the Advanced Etch Technology for Nanopatterning II, (2013).
4. A. Paranjpe, B. Druz, K. Rook and N. Srinivasan, (Google Patents, 2018).
5. J. W. Coburn and H. F. Winters, Journal of Applied physics **50** (5), 3189-3196 (1979).
6. T. Matsuura, J. Murota, Y. Sawada and T. Ohmi, Applied physics letters **63** (20), 2803-2805 (1993).
7. C. Kauppinen, S. A. Khan, J. Sundqvist, D. B. Suyatin, S. Suihkonen, E. I. Kauppinen and M. Sopanen, Journal of Vacuum Science & Technology A: Vacuum, Surfaces, and Films **35** (6), 060603 (2017).
8. Y. Lee and S. M. George, ACS nano **9** (2), 2061-2070 (2015).
9. S. Park, W. Lim, B. Park, H. Lee, J. Bae and G. Yeom, Electrochemical and Solid-State Letters **11** (4), H71-H73 (2008).
10. M. Konh, C. He, X. Lin, X. Guo, V. Pallem, R. L. Opila, A. V. Teplyakov, Z. Wang and B. Yuan, Journal of Vacuum Science & Technology A: Vacuum, Surfaces, and Films **37** (2), 021004 (2019).
11. J. W. Park, D. San Kim, W. O. Lee, J. E. Kim and G. Y. Yeom, Nanotechnology **30** (8), 085303 (2018).
12. E. Vogli, D. Metzler and G. S. Oehrlein, Applied Physics Letters **102** (25), 253105 (2013).
13. N. R. Johnson, H. Sun, K. Sharma and S. M. George, Journal of Vacuum Science & Technology A: Vacuum, Surfaces, and Films **34** (5), 050603 (2016).
14. W. Lu, Y. Lee, J. C. Gertsch, J. A. Murdzek, A. S. Cavanagh, L. Kong, J. s. A. del Alamo and S. M. George, Nano letters **19** (8), 5159-5166 (2019).
15. K. J. Kanarik, S. Tan, W. Yang, T. Kim, T. Lill, A. Kabansky, E. A. Hudson, T. Ohba, K. Nojiri and J. Yu, Journal of Vacuum Science & Technology A: Vacuum, Surfaces, and Films **35** (5), 05C302 (2017).
16. N. D. Altieri, J. K.-C. Chen, L. Minardi and J. P. Chang, Journal of Vacuum Science & Technology A: Vacuum, Surfaces, and Films **35** (5), 05C203 (2017).
17. X. Gu, Y. Kikuchi, T. Nozawa and S. Samukawa, Journal of Physics D: Applied Physics **47** (32), 322002 (2014).

18. E. Mohimi, X. I. Chu, B. B. Trinh, S. Babar, G. S. Girolami and J. R. Abelson, ECS Journal of Solid State Science and Technology **7** (9), P491-P495 (2018).
19. X. Lin, M. Chen, A. Janotti and R. Opila, Journal of Vacuum Science & Technology A: Vacuum, Surfaces, and Films **36** (5), 051401 (2018).
20. N. R. Johnson and S. M. George, ACS Applied Materials & Interfaces **9** (39), 34435-34447 (2017).
21. J. A. Levinson, E. S. Shaqfeh, M. Balooch and A. V. Hamza, Journal of Vacuum Science & Technology A: Vacuum, Surfaces, and Films **15** (4), 1902-1912 (1997).
22. J. P. Chang, J. C. Arnold, G. C. Zau, H.-S. Shin and H. H. Sawin, Journal of Vacuum Science & Technology A: Vacuum, Surfaces, and Films **15** (4), 1853-1863 (1997).
23. J. P. Chang and H. H. Sawin, Journal of Vacuum Science & Technology A: Vacuum, Surfaces, and Films **15** (3), 610-615 (1997).
24. X. Sang and J. P. Chang, Journal of Physics D: Applied Physics **53**, 183001 (2020).
25. R. M. Martin and J. P. Chang, Journal of Vacuum Science & Technology A: Vacuum, Surfaces, and Films **27** (2), 224-229 (2009).
26. J. K.-C. Chen, N. D. Altieri, T. Kim, T. Lill, M. Shen and J. P. Chang, Journal of Vacuum Science Technology A: Vacuum, Surfaces, Films **35** (5), 05C304 (2017).
27. J. K.-C. Chen, N. D. Altieri, T. Kim, E. Chen, T. Lill, M. Shen and J. P. Chang, Journal of Vacuum Science Technology A: Vacuum, Surfaces, Films **35** (5), 05C305 (2017).
28. N. Matsunami, Y. Yamamura, Y. Itikawa, N. Itoh, Y. Kazumata, S. Miyagawa, K. Morita, R. Shimizu and H. Tawara, Atomic Data & Nuclear Data Tables **31** (1), 1-80 (1984).
29. E. S. Lambers, C. Dykstal, J. M. Seo, J. E. Rowe and P. H. Holloway, Oxidation of metals **45** (3-4), 301-321 (1996).
30. X. Sang and J. P. Chang, (2020).
31. J. P. Perdew, K. Burke and M. Ernzerhof, Physical review letters **77** (18), 3865 (1996).
32. G. Kresse and J. Furthmüller, Physical review B **54** (16), 11169 (1996).
33. P. E. Blöchl, Physical review B **50** (24), 17953 (1994).
34. G. Kresse and D. Joubert, Physical review b **59** (3), 1758 (1999).
35. G. Kresse and J. Furthmüller, Computational materials science **6** (1), 15-50 (1996).
36. A. H. Larsen, J. J. Mortensen, J. Blomqvist, I. E. Castelli, R. Christensen, M. Dułak, J. Friis, M. N. Groves, B. Hammer and C. Hargus, Journal of Physics: Condensed Matter **29** (27), 273002 (2017).
37. H. Edwards and A. Knowles, Journal of molecular structure **268** (1-3), 13-22 (1992).